AGU PUBLICATIONS

Geophysical Research Letters

RESEARCH LETTER
10.1002/2017GL076790

Key Points:
- Broadband station deployed on Juan Fernandez Island detected *T* phases from South American earthquakes
- *T* phase energy fluxes of the Valparaíso and Illapel earthquakes depend on their depths along the dip and the bathymetry along their travel paths
- Tectonic characteristics near the trench control the *T* phase efficiencies of interplate thrust events

Supporting Information:
- Supporting Information S1
- Table S1

Correspondence to:
M. Sáez,
msaez@dgf.uchile.cl

Citation:
Sáez, M., & Ruiz, S. (2018). Controls on the *T* phase energy fluxes recorded on Juan Fernandez Island by continental seismic wave paths and Nazca bathymetry. *Geophysical Research Letters*, *45*, 2610–2617. https://doi.org/10.1002/2017GL076790

Received 12 DEC 2017
Accepted 22 FEB 2018
Accepted article online 28 FEB 2018
Published online 23 MAR 2018

©2018. American Geophysical Union. All Rights Reserved.

Controls on the *T* Phase Energy Fluxes Recorded on Juan Fernandez Island by Continental Seismic Wave Paths and Nazca Bathymetry

Miguel Sáez[1,2] **and Sergio Ruiz**[1]

[1]Geophysics department, Universidad de Chile, Santiago, Chile, [2]Geology department, Universidad de Chile, Santiago, Chile

Abstract *T* phases from 54 South American earthquakes with $M_w > 5.2$ are observed at a broadband station on Juan Fernandez Island. We computed the *T* phase energy flux (TPEF) values of the seismograms. The TPEF values show a large dispersion that can be explained by considering the tectonic characteristics of the South American plate and the Nazca plate bathymetry. The TPEFs generated by the 2015 Illapel and 2017 Valparaíso seismic sequences were controlled by the positions of the interface events along the dip. The central and downdip interplate earthquakes were more efficient in the generation of *T* phases than the near-trench interplate earthquakes (depths of <15 km). The variations in the generation efficiency with depth are explained by the continental raypaths of the body waves and the incidence angles of waves entering the sound fixing and ranging channel. Additionally, we observed differences in the TPEFs from both earthquake sequences that were controlled by seamounts atop the Nazca plate along the *T* phase paths.

1. Introduction

Since 2015, the National Seismological Center (CSN) has operated the continuously recording broadband station VA04 on Juan Fernandez Island (JFI), which is located 700 km from the South American coast. Station VA04 has consequently recorded most of the larger events that occurred throughout South America (see Figure 1a). Due to the large hypocentral distances between these events and station VA04, the resulting high-frequency body waves are strongly attenuated; nevertheless, *T* phases are clearly observed in the records (Matsumoto et al., 2016). *T* phases are high-frequency acoustic waves (2–8 Hz) that are generated by the conversion of seismic waves trapped within the sound fixing and ranging (SOFAR) channel (Talandier & Okal, 1998). The SOFAR channel is a low-velocity channel located 1,200 m below the sea surface that acts as a waveguide for *T* phases, thereby allowing them to travel long distances without anelastic attenuation (Thorp, 1965). The low attenuation property of *T* phases has been utilized to study the source properties of distant earthquakes (Okal & Talandier, 1997), underwater landslides (Fryer et al., 2004), and low-magnitude seismic swarms (Ito et al., 2012) and to differentiate between nuclear explosions and earthquakes (Talandier & Okal, 2001). On the receiver side, *T* phases are converted from acoustic to seismic waves, being strongly attenuated by continental raypaths and the conversion process (Kosuga, 2011; Walker et al., 1992). Despite this, Buehler and Shearer (2015) showed that it is possible to observe them at coastal stations using stacking methods. For simplicity, we refer to seismic waves recorded on seismograms after the conversion process as "*T* phases." Despite its multiple uses, the mechanism through which *T* phases are generated is a complex process that is not well understood; this is primarily due to differences in a multitude of factors, including variations in the bathymetry, sizes, and types of earthquakes; continental and oceanic raypaths; and frequency content (Williams et al., 2006), which affect their formation.

We analyzed 54 earthquakes with magnitudes larger than M_w 5.2 (Table S1 in the supporting information). These earthquakes are associated with the subduction of the Nazca plate beneath the South American plate and primarily occur along the plate interface, along which Lay et al. (2012) proposed three different seismic domains that generate high-frequency content. Events from shallower depths (<15 km) are characterized by source spectra with low high-frequency contents (Ye et al., 2013), and they are deficient in the generation of *T* phases (Okal et al., 2003). Meanwhile, events generated at moderate depths (15–30 km) along the central plate interface have modest high-frequency content in their source spectra. Finally, interface events from greater downdip depths (35–60 km) are characterized by earthquakes with source spectra rich in high-frequency content (Lay et al., 2012; Ye et al., 2013, among others). In this study, we compared the *T* phase energy flux (TPEF) values and high-frequency seismic source spectrum content recorded at broadband

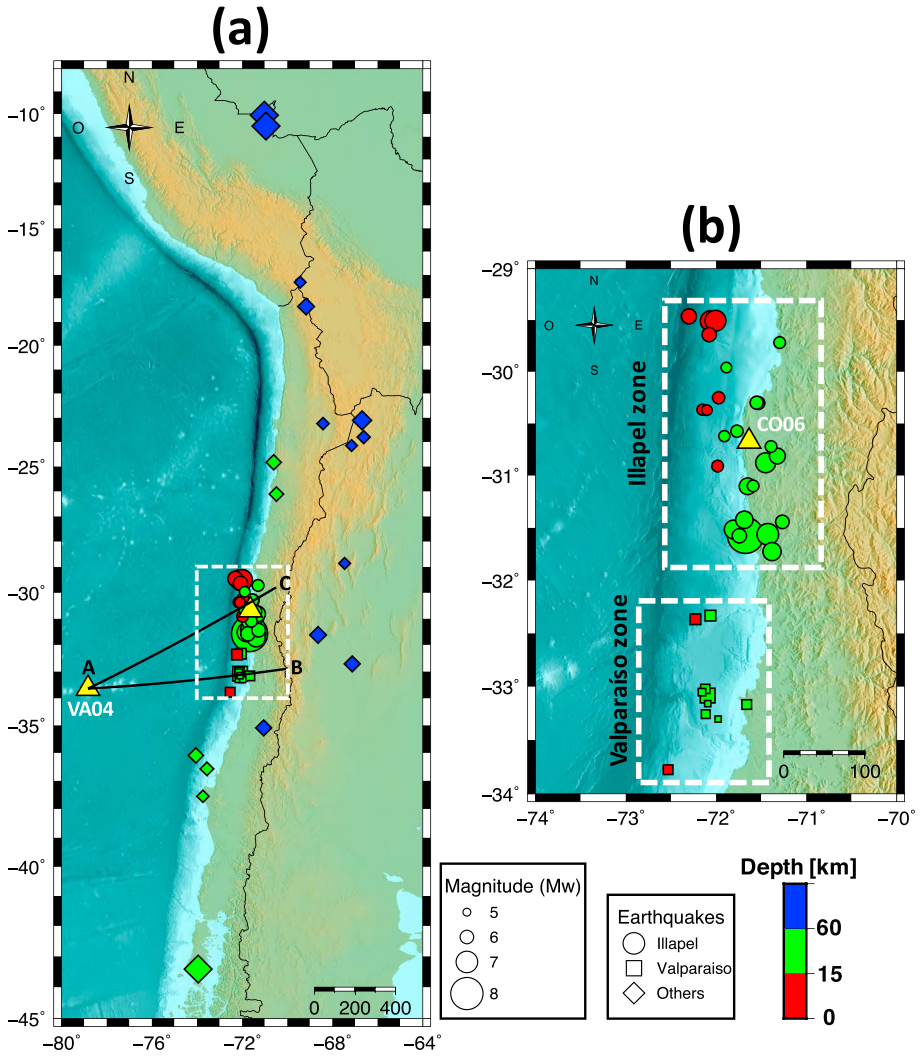

Figure 1. Spatial distribution of the 54 earthquakes analyzed in this study. The sizes and colors of the markers are proportional to the M_w and depth of each event, respectively. (a) South American earthquakes ($M_w > 5.2$) that occurred between February 2015 and May 2017 recorded by station VA04 on Juan Fernandez Island and station CO06 in the city of Coquimbo. The largest events considered are the 2015 Illapel M_w 8.3, 2017 Chiloé M_w 7.6, 2015 deep Peru M_w 7.6, and 2017 Valparaíso M_w 6.9 earthquakes. (b) Magnified view of the white box shown in (a). The circles are events associated with the 2015 Illapel seismic sequence, and the squares represent the 2017 Valparaíso seismic sequence.

station VA04 on JFI with those recorded at the coastal broadband station CO06 (see Figure 1). We focused on the seismic sequences of the 2015 M_w 8.3 Illapel and 2017 M_w 6.9 Valparaíso earthquakes (Ruiz et al., 2016; Ruiz, Aden-Antoniow, et al., 2017) because their foreshocks and aftershocks were located over the entire plate interface. Our results show that the TPEFs observed at JFI depend on the body waves produced by continental raypaths, the incidence angle into the SOFAR channel and the bathymetry of the Nazca plate.

2. Data and Methodology

2.1. JFI and Chilean Coastal CSN Broadband Stations

Stations VA04 and CO06 are located on JFI and on the Chilean coast at 90 and 200 m above sea level, respectively (see Figure 1). We considered South American earthquakes that occurred between February 2015 and May 2017, during which time VA04 was operating continuously. Figure 1a shows the epicenters from the CSN catalog for the Chilean events and those from the United States Geological Survey catalog for the other earthquakes. Table S1 shows the magnitude (ranging from M_w 5.2 to M_w 8.3), epicenter location, and focal

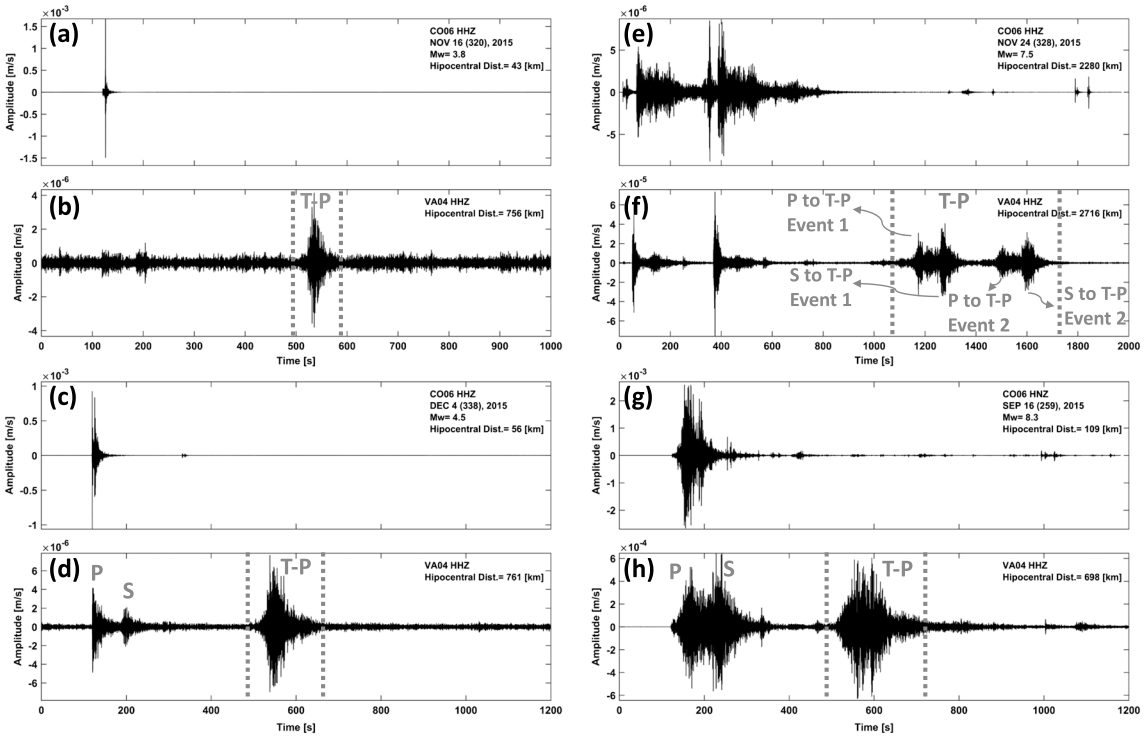

Figure 2. Four seismograms filtered between 2 and 8 Hz of earthquakes recorded simultaneously at stations VA04 and CO06. (a, c, e, and g) Seismograms recorded at station CO06. (b, d, f, and h) Seismograms recorded at station VA04. The gray dashed lines represent the windows that contain the *T* phases (T-P).

depth (ranging from 10 to 620 km) of each event. Stations VA04 and C006 are equipped with a broadband Trillium 120-s period sensor, a Marmot data logger system, and a Quanterra Q330 digitizer. The broadband stations recorded continuously at a rate of 100 samples per second.

2.2. *T* Phases Observed at the JFI and Chilean Coastal Stations

We filtered the up-down components using a fourth-order Butterworth band-pass filter with corner frequencies of 2 and 8 Hz. Figure 2 shows filtered traces generated in VA04 and CO06 stations for four different earthquakes. The *T* phases recorded at station VA04 have amplitudes greater than or similar to those of *P* or *S* waves (Figures 2b and 2d). The *T* phases of the deep Peru 2015 earthquakes (Ruiz, Tavera, et al., 2017) exhibit conversions from both *P* and *S* phases to *T* phases (Figure 2f), similar to the conversions from the deep Bolivian 1994 M_w 8.2 earthquake observed by Okal and Talandier (1997) at other broadband stations placed on islands throughout the Pacific Ocean. Although the distance between station CO06 and the 1,200 m isobath is only 16 km, the *T* phases are strongly attenuated by the continental raypath, and thus, it is impossible to distinguish their arrivals in the filtered traces (Figures 2a, 2c, 2e, and 2g).

2.3. *T* Phase Energy Flux

The TPEF generated by a *T* phase at a receiver is defined as follows (Okal et al., 2003):

$$\mathrm{TPEF} = \rho\alpha\int_W [\dot{u}(t)]^2 dt \tag{1}$$

where $\dot{u}(t)$ is the vertical ground velocity motion, *W* is the *T* phase duration, and ρ and α are the density and *P* wave velocity at the site where the station is located, respectively.

After filtering the records, we followed the steps listed hereafter to calculate the TPEF.

1. We calculated the theoretical arrival times of the *T* phases. Considering the travel time of *P* and *S* waves from the hypocenter to the continental slope and the travel times of *T* phases in the SOFAR channel, we used average velocities of 8, 4.6, and 1.484 km/s, respectively (Talandier & Okal, 1998).
2. Utilizing the theoretical *T* phase arrival time at station VA04, we visually selected the *T* phase time windows. We performed this process manually due to the frequent seismicity detected at VA04 during the seismic sequences of 2015 Illapel and 2017 Valparaíso earthquakes.

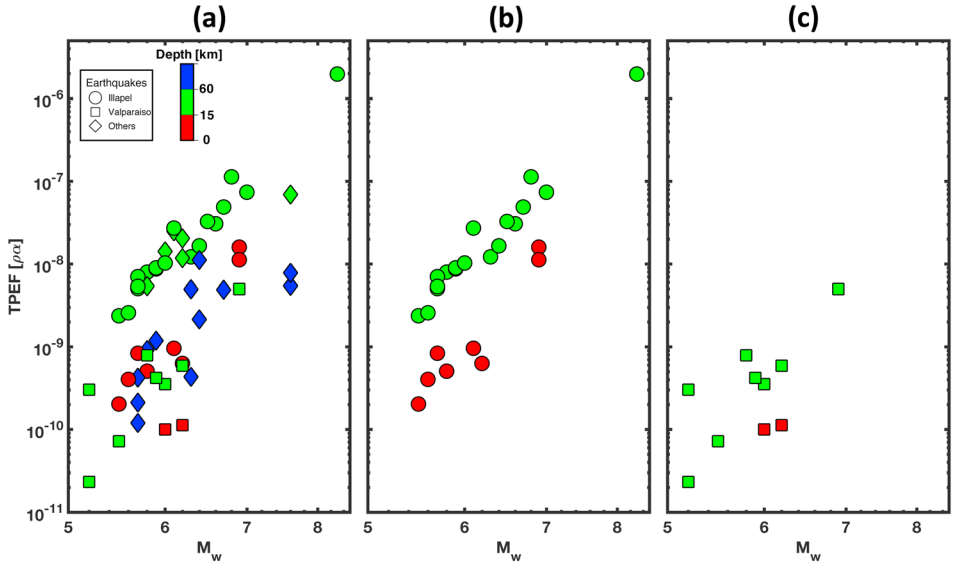

Figure 3. *T* phase energy flux (TPEF) as a function of the magnitude M_w. (a) TPEF versus M_w for the 54 South American earthquakes shown in Figure 1. (b) TPEF versus M_w for the Illapel events. (c) TPEF versus M_w for the Valparaíso events.

3. We divided the *T* phase records into windows with a length of 1 s and calculated their root mean square (rms) in each available window, thereby generating an rms curve.
4. The rms curve was normalized according to its maximum value and then smoothed using a moving average of 5 points (Figure S1 in the supporting information).
5. We calculated the TPEF according to equation (1) by considering the *T* phase duration (*W*) where the rms-normalized amplitude is equal to or greater than 0.6 as the record portion (Figure S1). Finally, our computed TPEF values are normalized by ρ and α.

3. Results

3.1. TPEF Efficiency

Figure 3a shows the TPEF values generated at station VA04 by the earthquakes shown in Figure 1a. The TPEF values scale according to the event magnitudes, as was proposed originally by Okal et al. (2003). The data dispersion between the TPEF and the magnitude decreases when we separate the values associated with each seismic sequence (see Figures 3b and 3c). The Illapel and Valparaíso seismic sequences show that near-trench earthquakes (<15 km depth) have TPEF values lower than those of deeper earthquakes (15–60 km depth). Intraplate intermediate-depth earthquakes (>60 km depth) have a higher TPEF dispersion, but this can be explained by the diverse depths and zones in which those events occurred (Figure 1). In addition, the Valparaíso seismic sequence generated smaller TPEF values than the Illapel earthquakes, even though their epicentral distances to JFI are smaller.

3.2. High-Frequency Fourier Spectrum Variations

We computed the Fourier amplitude spectra of the Illapel earthquakes recorded at stations VA04 and CO06 by considering time windows beginning with the first *P* wave arrivals and ending 30 s after the *S* wave arrivals. We chose this time window because of the relationship between the body waves and the conversion from seismic to acoustic waves (Balanche et al., 2009; Talandier & Okal, 1998). To compare the events with different magnitudes, we decided to normalize the Fourier spectra at 1 Hz, as their corner frequencies are all less than 1 Hz. The Fourier spectra associated with the Illapel events recorded at station VA04 (Figure 4a) show an important frequency content between 2 and 8 Hz independent of the event depths. Meanwhile, the Fourier spectra associated with the Illapel earthquakes recorded at station CO06 show variations in the frequency content with respect to their focal depths. The shallower events (<15 km depth) have lower high-frequency spectral amplitudes between 2 and 8 Hz compared with those of the deeper events (15–60 km depth).

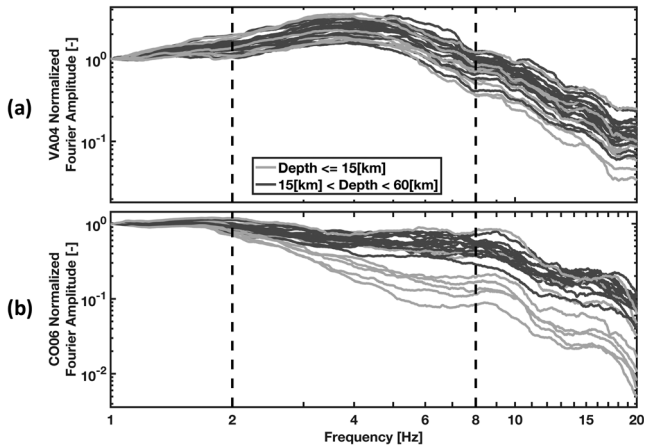

Figure 4. Fourier amplitude spectra of the Illapel earthquakes normalized to 1 Hz. (a) VA04 records. (b) CO06 records. Frequencies between 2 and 8 Hz for near-trench interface events are more attenuated at station CO06 than at station VA04. The gray and black lines represent normalized Fourier amplitude of near trench (depth $\leq$ 15 km) and central and downdip earthquakes (15 km $<$ depth $\leq$ 60), respectively.

4. Discussion

4.1. High-Frequency Variations in the Plate Interface Events Along Dip

Okal et al. (2003) first suggested the presence of a dip-dependent variation in the efficiencies of generated *T* phases after observing lower TPEF values for tsunami earthquakes. According to Okal (2008), these types of events are deficient in the generation of *T* phases due to their low spectral frequency contents above 1 Hz. This dip-dependent difference in the source spectra for plate interface events was corroborated by Lay et al. (2012), and other authors, who studied the source spectra of recent megathrust subduction earthquakes. In this study, we compared the Fourier spectra of the 2015 Illapel earthquakes in the frequency band from 2 to 8 Hz. Figure 4 shows different high-frequency properties between the broadband records of stations VA04 and CO06. While the Fourier spectra recorded at VA04 from the shallow, central, and downdip interface events do not display evident differences, the Fourier spectra for the shallower earthquakes recorded at CO06 exhibit a lower high-frequency spectral content than the deeper ones. We propose that the greater high-frequency attenuation observed at station CO06 is associated with the continental raypaths of the body waves. The shallower earthquakes generated body waves that traveled from the near-trench area to the coast through an eroded and fractured wedge that probably serves as a low-pass filter (Figure 5a). This wedge has previously been observed along the Chilean subduction zone, and it is characterized by a low-velocity zone relative to the continental basement (Contreras-Reyes et al., 2012, 2014; León-Ríos et al., 2016). Meanwhile, the central and downdip interplate events generated body waves that traveled through the continental basement (Figure 5a), which would attenuate high-frequency waves relatively less. In the case of station VA04, the raypaths of the body waves' path did not travel through the eroded and fractured wedge because they traveled directly to JFI without traversing the South American plate (Figure 5a). We propose that the observed deficiency of *T* phases from shallower earthquakes can be partially explained by the high-frequency attenuation of body waves produced by their paths through the wedge to the continental slope where the seismic-acoustic conversion occurred.

4.2. *T* Phase Incidence Angles of Waves Entering the SOFAR Channel

Another reason for the depth-dependent *T* phase efficiency for the Valparaíso and Illapel earthquakes could be due to the incidence angles of the acoustic waves entering the SOFAR channel. The shallower events generated body waves with incidence angles that were almost vertical with respect to the continental slope; these waves would require a considerable number of reflections to reach a horizontal angle (~12°) suitable for penetrating the SOFAR channel (Okal, 2008; Talandier & Okal, 1998). These multiple reflections make the seismic-acoustic conversion relatively inefficient (Talandier & Okal, 1998). In contrast, the deeper events generated seismic rays with relatively horizontal incidence angles in comparison with the shallower earthquakes; these rays required fewer reflections to enter the SOFAR channel, and therefore, the generation of *T* phases was more efficient (Talandier & Okal, 1998). This explanation is schematically summarized in Figure 5b.

4.3. *T* Phase Path Bathymetry

Although the Valparaíso earthquakes have a smaller epicentral distance with respect to JFI (Figure 1), they generated TPEF values that were 1 order of magnitude lower than those of the Illapel earthquakes (Figures 3b and 3c). These different TPEF versus M_w trends can be explained by the complex Nazca bathymetry along the raypaths between the Valparaíso earthquakes and JFI compared with the smooth Nazca bathymetry between the Illapel earthquakes and JFI. The bathymetry along profile A′-B′ (Figure 5b) extracted from Becker et al. (2009) and Smith and Sandwell (1997) is characterized by several seamounts belonging to the Juan Fernandez Ridge with heights greater than 1,200 m (Figure 5c). These seamounts penetrate the SOFAR channel; therefore, they acted as a barrier to the propagation of *T* phases (Walker et al., 1992) between the 2017 Valparaíso earthquakes and JFI. In contrast, the smooth bathymetry of profile A′-C′ (Figure 5c) favored the efficient propagation of *T* phases between the 2015 Illapel earthquakes and JFI. Despite of the presence of

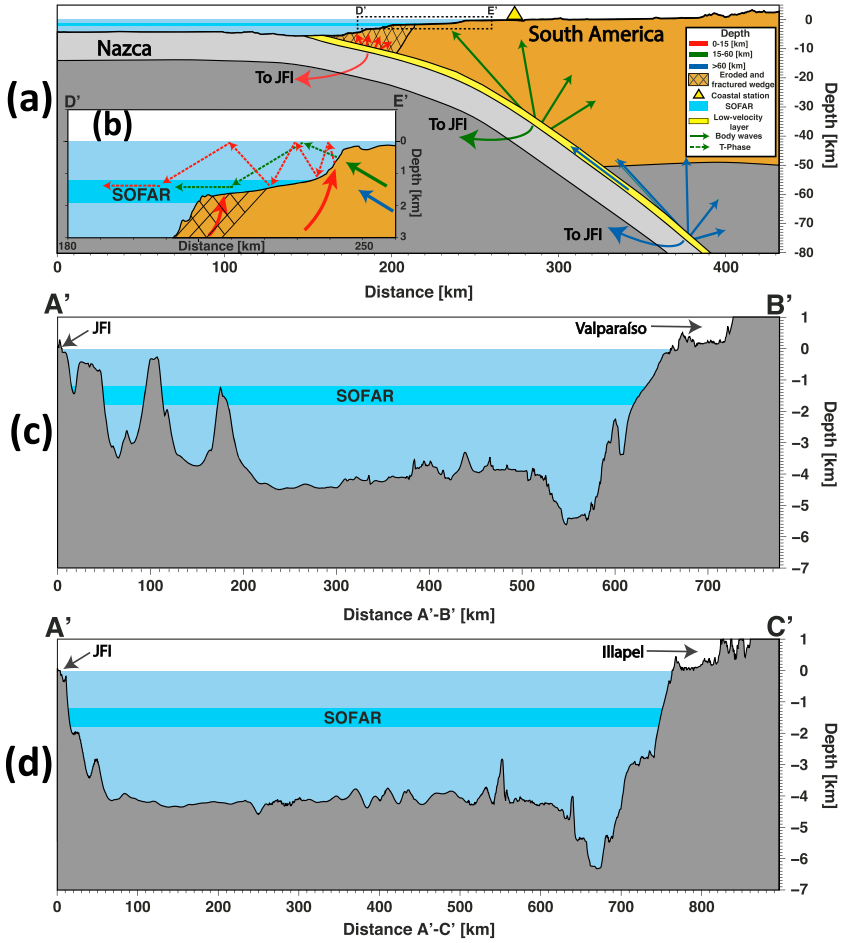

Figure 5. (a) Schematic illustration of body waves rays generated from near-trench interface events (red line), central and downdip interplate events (green line), and intraplate intermediate-depth earthquakes (blue line). The sound fixing and ranging channel is located at 1,200 m. The low-velocity layer is based in the scheme suggested for the Northern Chile by Garth and Rietbrock (2017). (b) Scheme of the generation of *T* phases. (c) Bathymetry of profile A′-B′ in Figure 1b representative of the Valparaíso-Juan Fernandez Island (JFI) raypaths (Figure 1b). (d) Bathymetry of profile A′-C′ in Figure 1b representative of the Illapel-JFI raypaths (Figure 1b).

seamounts along profile A′-B′, we were not able to detect reversed propagation of *T* phases (Obara & Maeda, 2009) due to the high rate of aftershocks detected during the 2017 Valparaíso seismic sequence.

4.4. Intraplate Intermediate-Depth Events

Intraplate intermediate-depth earthquakes occur at depths greater than 60 km throughout most of the South American subduction zone. The presence of a low-velocity layer at the top of the subducting oceanic crust (Garth & Rietbrock, 2017; Martin et al., 2003) and the scattering due to small-scale heterogeneities within the subducted plate (Furumura & Kennett, 2005) have been proposed as waveguides for high frequency. Despite this, the TPEFs calculated for intraplate intermediate-depth events are similar to those of the shallower Illapel earthquakes and the Valparaíso central and downdip interface events (Figure 3a). Additional data and research are needed to interpret the TPEFs values of these types of events, especially because we considered events located in different zones (Figure 1a) characterized by different conditions of *T* phase generation and different Nazca bathymetry paths.

5. Conclusions

We showed that *T* phases produced by various South American earthquakes were recorded at the broadband station deployed on JFI. The situation was different for the coastal station CO06, where very weak *T* phases

were recorded due to strong attenuation along the continental raypath. The TPEFs generated by the South American earthquakes recorded at JFI increased with M_w. For the 2015 Illapel and 2017 Valparaíso seismic sequences, the TPEF values were controlled mainly by the Nazca bathymetry along the oceanic raypaths and the hypocentral depths of the earthquakes. The complex bathymetry between the 2017 Valparaíso earthquakes and JFI reduced the continuity of the SOFAR channel relative to that along the raypaths from the 2015 Illapel earthquakes to JFI; thus, the *T* phases were able to propagate more efficiently between the latter. In addition, we observed that the *T* phase efficiency varied with the dip. The central and downdip earthquakes (depths ranging from 15 to 60 km) were more efficient in the generation of *T* phases than near-trench earthquakes (depths less than 15 km). This depth dependency of the efficiency can be explained by two reasons: (1) higher seismic wave attenuation along continental wedge raypaths in comparison with those through the continental basement and (2) the incidence angles of waves entering the SOFAR channel. We expect that future seismicity in South America will generate *T* phases that follow the pattern exposed herein, for which JFI can be used as a natural place for continuous monitoring.

Acknowledgments
We thank CSN, National Seismological Center of the Universidad de Chile, for providing us the raw data of VA04 and CO06 stations, which are available at CSN or Incorporated Research Institutions for Seismology Data Management (IRIS). Miguel Sáez thanks the scholarship PCHA/Doctorado Nacional/2017-21171480, granted by CONICYT. This work was partially funded by PRS (Programa de Riesgo Sísmico, Universidad de Chile) and FONDECYT 1170430. We also thank R. Madariaga for his helpful advice and the two anonymous reviewers whose comments helped to improve this article.

References

Balanche, A., Guennou, C., Goslin, J., & Mazoyer, C. (2009). Generation of hydroacoustic signals by oceanic subseafloor earthquakes: A mechanical model. *Geophysical Journal International*, *177*(2), 476–480. https://doi.org/10.1111/j.1365-246X.2009.04146.x

Becker, J. J., Sandwell, D. T., Smith, W. H. F., Braud, J., Binder, B., Depner, J., et al. (2009). Global bathymetry and elevation data at 30 arc seconds resolution: SRTM30_PLUS. *Marine Geodesy*, *32*(4), 355–371. https://doi.org/10.1080/01490410903297766

Buehler, J. S., & Shearer, P. M. (2015). T phase observations in global seismogram stacks. *Geophysical Research Letters*, *42*, 6607–6613. https://doi.org/10.1002/2015GL064721

Contreras-Reyes, E., Becerra, J., Kopp, H., Reichert, C., & Díaz-Naveas, J. (2014). Seismic structure of the north-central Chilean convergent margin: Subduction erosion of a paleomagmatic arc. *Geophysical Research Letters*, *41*, 1523–1529. https://doi.org/10.1002/2013GL058729

Contreras-Reyes, E., Jara, J., Grevemeyer, I., Ruiz, S., & Carrizo, D. (2012). Abrupt change in the dip of the subducting plate beneath North Chile. *Nature Geoscience*, *5*(5), 342–345. https://doi.org/10.1038/ngeo1447

Fryer, G. J., Watts, P., & Pratson, L. F. (2004). Source of the great tsunami of 1 April 1946: A landslide in the upper Aleutian forearc. *Marine Geology*, *203*(3–4), 201–218. https://doi.org/10.1016/S0025-3227(03)00305-0

Furumura, T., & Kennett, B. L. N. (2005). Subduction zone guided waves and the heterogeneity structure of the subducted plate: Intensity anomalies in northern Japan. *Journal of Geophysical Research*, *110*, B10302. https://doi.org/10.1029/2004JB003486

Garth, T., & Rietbrock, A. (2017). Constraining the hydration of the subducting Nazca plate beneath Northern Chile using subduction zone guided waves. *Earth and Planetary Science Letters*, *474*, 237–247. https://doi.org/10.1016/j.epsl.2017.06.041

Ito, A., Sugioka, H., Suetsugu, D., Shiobara, H., Kanazawa, T., & Fukao, Y. (2012). Detection of small earthquakes along the Pacific-Antarctic Ridge from T-waves recorded by abyssal ocean-bottom observatories. *Marine Geophysical Research*, *33*(3), 229–238. https://doi.org/10.1007/s11001-012-9158-0

Kosuga, M. (2011). Localization of T-wave energy on land revealed by a dense seismic network in Japan. *Geophysical Journal International*, *187*(1), 338–354. https://doi.org/10.1111/j.1365-246X.2011.05143.x

Lay, T., Kanamori, H., Ammon, C. J., Koper, K. D., Hutko, A. R., Ye, L., et al. (2012). Depth-varying rupture properties of subduction zone megathrust faults. *Journal of Geophysical Research*, *117*, B04311. https://doi.org/10.1029/2011JB009133

León-Ríos, S., Ruiz, S., Maksymowicz, A., Leyton, F., Fuenzalida, A., & Madariaga, R. (2016). Diversity of the 2014 Iquique's foreshocks and aftershocks: Clues about the complex rupture process of a Mw 8.1 earthquake. *Journal of Seismology*, *20*(4), 1059–1073. https://doi.org/10.1007/s10950-016-9568-6

Martin, S., Rietbrock, A., Haberland, C., & Asch, G. (2003). Guided waves propagating in subducted oceanic crust. *Journal of Geophysical Research*, *108*(B11), 2536. https://doi.org/10.1029/2003JB002450

Matsumoto, H., Haralabus, G., Zampolli, M., & Özel, N. M. (2016). T-phase and tsunami pressure waveforms recorded by near-source IMS water-column hydrophone triplets during the 2015 Chile earthquake. *Geophysical Research Letters*, *43*, 12,511–12,519. https://doi.org/10.1002/2016GL071425

Obara, K., & Maeda, T. (2009). Reverse propagation of T waves from the Emperor seamount chain. *Geophysical Research Letters*, *36*, L08304. https://doi.org/10.1029/2009GL037454

Okal, E. A. (2008). The generation of T waves by earthquakes. *Advances in Geophysics*, *49*, 1–65. https://doi.org/10.1016/S0065-2687(07)49001-X

Okal, E. A., Alasset, P.-J., Hyvernaud, O., & Schindelé, F. (2003). The deficient T waves of tsunami earthquakes. *Geophysical Journal International*, *152*(2), 416–432. https://doi.org/10.1046/j.1365-246X.2003.01853.x

Okal, E. A., & Talandier, J. (1997). T waves from the great 1994 Bolivian deep earthquake in relation to channeling of S wave energy up the slab. *Journal of Geophysical Research*, *102*(B12), 27,421–27,437. https://doi.org/10.1029/97JB02718

Ruiz, S., Aden-Antoniow, F., Baez, J. C., Otarola, C., Potin, B., Campo, F., et al. (2017). Nucleation phase and dynamic inversion of the Mw 6.9 Valparaíso 2017 earthquake in Central Chile. *Geophysical Research Letters*, *44*, 10,290–10,297. https://doi.org/10.1002/2017GL075675

Ruiz, S., Klein, E., Del Campo, F., Rivera, E., Poli, P., Metois, M., et al. (2016). The seismic sequence of the 16 September 2015 Mw 8.3 Illapel, Chile, earthquake. *Seismological Research Letters*, *87*, 789–799.

Ruiz, S., Tavera, H., Poli, P., Herrera, C., Flores, C., Rivera, E., & Madariaga, R. (2017). The deep Peru 2015 doublet earthquakes. *Earth and Planetary Science Letters*, *478*, 102–109. https://doi.org/10.1016/j.epsl.2017.08.036

Smith, W. H. F., & Sandwell, D. T. (1997). Global Sea floor topography from satellite altimetry and ship depth soundings. *Science*, *277*(5334), 1956–1962. https://doi.org/10.1126/science.277.5334.1956

Talandier, J., & Okal, E. A. (1998). On the mechanism of conversion of seismic waves to and from T waves in the vicinity of island shores. *Bulletin of the Seismological Society of America*, *88*(2), 621–632.

Talandier, J., & Okal, E. A. (2001). Identification criteria for sources of T waves recorded in French Polynesia. *Pure and Applied Geophysics*, *158*, 567–603.

Thorp, W. H. (1965). Deep-ocean sound attenuation in the sub-and low-kilocycle-per-second region. *The Journal of the Acoustical Society of America*, *38*(4), 648–654. https://doi.org/10.1121/1.1909768

Walker, D. A., Mccreery, C. S., & Hiyoshi, Y. (1992). T-phase spectra, seismic moments, and tsunamigenesis. *Bulletin of the Seismological Society of America*, *82*(3), 1275–1305.

Williams, C. M., Stephen, R. A., & Smith, D. K. (2006). Hydroacoustic events located at the intersection of the Atlantis (30°N) and Kane (23°40′N) transform faults with the mid-Atlantic ridge. *Geochemistry, Geophysics, Geosystems*, *7*, Q06015. https://doi.org/10.1029/2005GC001127

Ye, L., Lay, T., & Kanamori, H. (2013). Ground shaking and seismic source spectra for large earthquakes around the megathrust fault offshore of northeastern Honshu, Japan. *Bulletin of the Seismological Society of America*, *103*(2B), 1221–1241. https://doi.org/10.1785/0120120115